Study of $D^+ \to K_S^0 K^*(892)^+$ in $D^+ \to K_S^0 K_S^0 \pi^+$

M. Ablikim *et al.*[*]
(BESIII Collaboration)

(Received 4 September 2024; accepted 9 October 2024; published 8 November 2024)

Using a data sample of e^+e^- collisions corresponding to an integrated luminosity of 7.93 fb^{-1} collected with the BESIII detector at the center-of-mass energy 3.773 GeV, we perform the first amplitude analysis of the decay $D^+ \to K_S^0 K_S^0 \pi^+$. The absolute branching fraction of $D^+ \to K_S^0 K_S^0 \pi^+$ is measured to be $(2.97 \pm 0.09_{\mathrm{stat}} \pm 0.05_{\mathrm{syst}}) \times 10^{-3}$. The dominant intermediate process is $D^+ \to K_S^0 K^*(892)^+$, whose branching fraction is determined to be $(8.72 \pm 0.28_{\mathrm{stat}} \pm 0.15_{\mathrm{syst}}) \times 10^{-3}$, including all the $K^*(892)^+$ decays.

DOI: 10.1103/PhysRevD.110.092006

I. INTRODUCTION

The masses of the charmed mesons, approximately 2 GeV/c^2, fall within a region where nonperturbative quantum chromodynamics (QCD) is no longer negligible. This presents a challenge for studying the hadronic transitions of charmed mesons. The lightest charmed mesons $D^{0(+)}$ can only decay through weak interactions, and the related amplitudes are dominated by two-body processes, i.e. $D \to VP$, $D \to PP$, $D \to SP$, and $D \to VV$ decays, where V, S, and P denote vector, scalar, and pseudoscalar mesons, respectively. In particular, the $D \to VP$ decays offer cleaner opportunities than other two-body processes for clarifying the nonperturbative mechanism of charmed meson decays [1–3]. Compared to the $D \to SP$ decay, the VP system presents a more well-defined quark content of the vector meson than that of the scalar state, whose quark content is still a matter of controversy and is further complicated by significant long-distance rescattering effects [4–8]. The VP system also can be more favorably described by the theoretical framework than the PP and VV systems, due to the multiple-amplitude composition of some P states [2,3] and the polarization in VV systems [9].

While most of the theoretical predicted branching fractions (BFs) of $D \to VP$ decays are consistent with experimental measurements, that for $D^+ \to K_S^0 K^*(892)^+$ shows inconsistency. The $D^+ \to K_S^0 K^*(892)^+$ decay is one of the most important singly-Cabibbo-suppressed (SCS) $D \to VP$ decays [10,11], which can be mediated via color-favored, W-annihilation, and penguin diagrams [2] as shown in Fig. 1. The predicted and measured values of the BF $\mathcal{B}(D^+ \to K_S^0 K^*(892)^+)$ are listed in Table I, where predicted BFs of the decay $D^+ \to K_S^0 K^*(892)^+$ are from the pole model [12], the factorization-assisted topological-amplitude [FAT (mix)] approach with $\rho - \omega$ mixing [13], the topological diagram approach (TDA) with only tree level amplitude [denoted as TDA (tree)] [1], including QCD-penguin amplitudes [denoted as TDA (QCD-penguin)] [2], and the updated analysis of the two-body $D \to VP$ decays within the framework of the TDA [14].

The information of two-body decays can be extracted by performing an amplitude analysis of decays with multiple-body final states via intermediate resonance. The BESIII Collaboration has measured the BF of $D^+ \to K_S^0 K^*(892)^+$ to be $(8.69 \pm 0.40_{\mathrm{stat}} \pm 0.64_{\mathrm{syst}} \pm 0.51_{\mathrm{Br}}) \times 10^{-3}$ in the amplitude analysis of $D^+ \to K^+ K_S^0 \pi^0$ [11] using a data sample corresponding to an integrated luminosity of 2.93 fb^{-1} at the center-of-mass energy 3.773 GeV, where the third uncertainty is due to the quoted uncertainty of $\mathcal{B}(D^+ \to K^+ K_S^0 \pi^0)$ [10]. This result differs from the theoretical predictions in Refs. [1,2,13] by about 4σ. However, the result is consistent with the predictions based on Refs. [12,14], which suffers from large uncertainties. Therefore, a more precise measurement of $D^+ \to K_S^0 K^*(892)^+$ is needed to provide a more stringent test of the models and to deepen our understanding of the dynamics of charmed meson decays. A clearer environment is expected to be offered in the $D^+ \to K_S^0 K_S^0 \pi^+$ decay without the interference from $D^+ \to K^+ K^*(892)^0$ in $D^+ \to K^+ K_S^0 \pi^0$.

The $D^+ \to K_S^0 K_S^0 \pi^+$ decay has been previously observed by the BESIII Collaboration with a BF of $\mathcal{B}(D^+ \to K_S^0 K_S^0 \pi^+) = (2.70 \pm 0.05_{\mathrm{stat}} \pm 0.12_{\mathrm{syst}}) \times 10^{-3}$ [15]. Using a data sample of e^+e^- collisions corresponding to an integrated luminosity of 7.93 fb^{-1} [16–18] collected by the

[*]Full author list given at the end of the article.

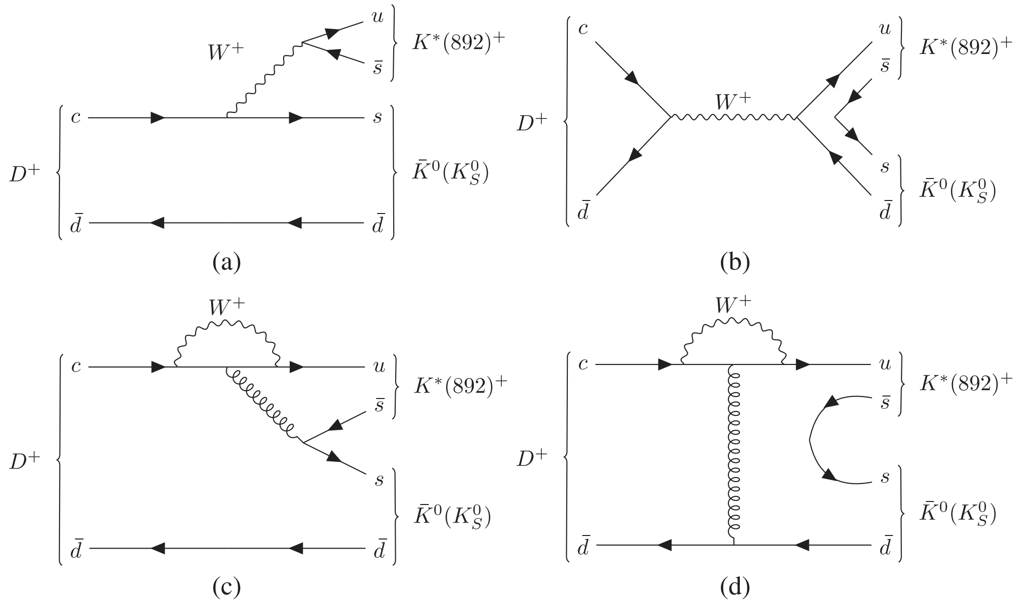

FIG. 1. Topological diagrams contributing to the decay $D^+ \to K_S^0 K^*(892)^+$ with (a) color allowed external W-emission tree diagram, (b) W-annihilation diagram, (c) color suppressed external W-emission QCD-penguin diagram, and (d) QCD-penguin exchange diagram.

BESIII detector [19] at the center-of-mass energy 3.773 GeV, we performed the first amplitude analysis and the absolute BF measurement of the SCS decay $D^+ \to K_S^0 K_S^0 \pi^+$. Charge-conjugate states are implied throughout this paper, allowing for the signal-side decay $D^- \to K_S^0 K_S^0 \pi^-$.

II. DETECTOR AND MONTE CARLO SIMULATION

The BESIII detector [19] records symmetric e^+e^- collisions provided by the BEPCII storage ring [20] in the center-of-mass energy range from 2.00 to 4.95 GeV, with a peak luminosity of $1 \times 10^{33}\ \mathrm{cm}^{-2}\,\mathrm{s}^{-1}$ achieved at $\sqrt{s} = 3.77$ GeV. BESIII has collected large data samples in this energy region [21–23]. The cylindrical core of the BESIII detector covers 93% of the full solid angle and consists of a helium-based multilayer drift chamber (MDC), a plastic scintillator time-of-flight system (TOF), and a CsI(Tl) electromagnetic calorimeter (EMC), which are all enclosed in a superconducting solenoidal magnet providing a 1.0 T magnetic field. The solenoid is supported by an octagonal flux-return yoke with resistive plate counter muon identification modules interleaved with steel. The charged-particle momentum resolution at 1 GeV/c is 0.5%, and the dE/dx resolution is 6% for electrons from Bhabha scattering. The EMC measures photon energies with a resolution of 2.5% (5%) at 1 GeV in the barrel (end cap) region. The time resolution in the TOF barrel region is 68 ps, while that in the end cap region was 110 ps. The end cap TOF system was upgraded in 2015 using multigap resistive plate chamber technology, providing a time resolution of 60 ps, which benefits 63% of the data used in this analysis [24].

TABLE I. Theoretical predictions of $\mathcal{B}(D^+ \to K_S^0 K^*(892)^+)$ and the previous experimental measurement.

Model	$\mathcal{B}(D^+ \to K_S^0 K^*(892)^+)$ $(\times 10^{-3})$
Pole [12]	6.2 ± 1.2
FAT (mix) [13]	5.5
TDA (tree) [1]	5.02 ± 1.31
TDA (QCD-penguin) [2]	4.90 ± 0.21
TDA [14]	7.90 ± 0.25
BESIII measurement [11]	$8.69 \pm 0.40_{\mathrm{stat}} \pm 0.64_{\mathrm{syst}} \pm 0.51_{\mathrm{BF}}$

Simulated inclusive Monte Carlo (MC) samples, with sizes that are 40 times the integrated luminosity of data, are produced with a GEANT4-based [25] MC simulation package, which includes the geometric description of the BESIII detector [26] and the detector response, and are used to determine detection efficiencies and to estimate backgrounds. The simulation models the beam energy spread and initial state radiation (ISR) in the e^+e^- annihilations with the generator KKMC [27]. The inclusive MC samples consist of the production of $D\bar{D}$ pairs, the non-$D\bar{D}$ decays of the $\psi(3770)$, the ISR production of the J/ψ and $\psi(3686)$ states, and the continuum processes incorporated in KKMC. All particle decays are modeled with EVTGEN [28] using BFs either taken from the Particle Data Group (PDG) [29], when available, or otherwise estimated with LUNDCHARM [30]. Final state radiation from charged final state particles is incorporated using PHOTOS [31]. In this work, two sets of MC samples, each comprising around 10×10^6 selected events, are used. The phase space (PHSP) MC sample is generated with a uniform distribution in phase space for the decay $D^+ \to K_S^0 K_S^0 \pi^+$, which is used to calculate the normalization factor of the probability density function (PDF) in the amplitude analysis. The signal MC sample, which is used to estimate the detection efficiencies, is generated according to the amplitude analysis results.

III. EVENT SELECTION

The process $e^+e^- \to \psi(3770) \to D^+D^-$ allows studies of D decays with a tag technique [32,33]. There are two types of samples used with the tag technique: single tag (ST) and double tag (DT). In the ST sample, only one D^- meson is reconstructed through one of six hadronic decay modes: $D^- \to K^+\pi^-\pi^-$, $K^+\pi^-\pi^-\pi^0$, $K_S^0\pi^-$, $K_S^0\pi^-\pi^0$, $K_S^0\pi^-\pi^-\pi^+$, and $K^+K^-\pi^-$. In the DT sample, the signal D^+ is reconstructed through $D^+ \to K_S^0 K_S^0 \pi^+$.

All charged tracks detected in the MDC must satisfy $|\cos\theta| < 0.93$, where θ is defined as the polar angle with respect to the z-axis, which is the symmetry axis of the MDC. For charged tracks not originating from K_S^0 decays, the distance of closest approach to the interaction point (IP) is required to be less than 1 cm in the transverse plane ($|V_{xy}|$) and less than 10 cm along the z-axis ($|V_z|$). Particle identification (PID) for charged tracks combines the $\mathrm{d}E/\mathrm{d}x$ measurement in the MDC with the time-of-flight measurement of the TOF detector to define the likelihood function $\mathcal{L}(h)(h = K, \pi)$ for each hadron (h) hypothesis. The charged kaons and pions are identified by comparing the likelihoods for the kaon and pion hypotheses, $\mathcal{L}(K) > \mathcal{L}(\pi)$ and $\mathcal{L}(\pi) > \mathcal{L}(K)$, respectively.

Each K_S^0 candidate is reconstructed from two oppositely charged tracks satisfying $|V_z| < 20$ cm. The two charged tracks are assigned as $\pi^+\pi^-$ without imposing PID. They are constrained to originate from a common vertex and are required to have an invariant mass $M_{\pi^+\pi^-}$ such that $|M_{\pi^+\pi^-} - m_{K_S^0}| < 12\ \mathrm{MeV}/c^2$, where $m_{K_S^0}$ is the known K^0 mass [29]. The decay length of the K_S^0 candidate is required to be greater than twice its resolution.

Photon candidates are selected using EMC showers. The deposited energy of each shower in the barrel region ($|\cos\theta| < 0.80$) and in the end cap region ($0.86 < |\cos\theta| < 0.92$) must be greater than 25 and 50 MeV, respectively. To exclude showers that originate from charged tracks, the angle subtended by the EMC shower and the position of the closest charged track at the EMC must be greater than 10° as measured from the IP. The difference between the EMC time and the event start time is required to be within [0, 700] ns to suppress electronic noise and showers unrelated to the event.

The π^0 candidates are reconstructed from photon pairs with invariant masses in the range $[0.115, 0.150]\ \mathrm{GeV}/c^2$, which corresponds to about 3 times the invariant mass resolution. We require that at least one photon comes from the barrel region of the EMC to improve the resolution. Furthermore, the π^0 candidates are constrained to the known π^0 mass [29] via a kinematic fit to improve their energy and momentum resolution.

Two variables, the beam-constrained mass M_{BC} and the energy difference ΔE, are used to identify the D^+ mesons,

$$M_{\mathrm{BC}} = \sqrt{E_{\mathrm{beam}}^2/c^4 - |\vec{p}_{D^+}|^2/c^2},$$
$$\Delta E = E_{D^+} - E_{\mathrm{beam}}, \tag{1}$$

where E_{beam} is the beam energy, and $\vec{p}_{D^+}$ and E_{D^+} are the total reconstructed momentum and energy of the D^+ candidate in the e^+e^- rest frame, respectively. The D^+ signals appear as a peak at the known D^+ mass [29] in the M_{BC} distribution and as a peak at zero in the ΔE distribution. The selection criteria of K_S^0 and π^+ on the signal side are the same as those on the tag side. For each tag mode, if there are multiple combinations, the one giving the minimum $|\Delta E_{\mathrm{tag}}|$ is retained for further analysis. The signal D^+ candidates are reconstructed from the particles that have not been used for the tagged D^- reconstruction. They are identified using the energy difference and the beam-constrained mass of the signal side, ΔE_{sig} and $M_{\mathrm{BC}}^{\mathrm{sig}}$, calculated similar to Eq. (1), with D^- replaced by D^+. If there are multiple combinations, the one giving the minimum $|\Delta E_{\mathrm{sig}}|$ is retained for further analysis.

IV. BACKGROUND STUDY

To increase the signal purity for amplitude analysis, we require $1.863 < M_{\mathrm{BC}}^{\mathrm{tag}} < 1.877\ \mathrm{GeV}/c^2$ for all tag modes, and $1.865 < M_{\mathrm{BC}}^{\mathrm{sig}} < 1.875\ \mathrm{GeV}/c^2$ and $-0.020 < \Delta E_{\mathrm{sig}} < 0.020$ GeV for the signal side. The boundaries of ΔE_{tag} requirements are listed in Table II. Then, we study the sources of background for $D^+ \to K_S^0 K_S^0 \pi^+$ by analyzing the inclusive MC samples. The main background is the decay $D^+ \to K_S^0 \pi^+\pi^-\pi^+$, since the combinatorial $\pi^+\pi^-$ pairs may accidentally satisfy the K_S^0 selection criteria and contribute as a peak around the D^+ mass in the M_{BC} distribution. This peaking background is estimated with events in the K_S^0 sideband region, defined as $0.020 < |M_{\pi^+\pi^-} - m_{K_S^0}| < 0.044\ \mathrm{GeV}/c^2$. The two-dimensional (2D) K_S^0 signal region is defined as the square region with

TABLE II. Requirements of ΔE_{tag} for different D^- tag modes.

D^- decay	ΔE_{tag} (GeV)
$K^+\pi^-\pi^-$	$(-0.025, 0.024)$
$K^+\pi^-\pi^-\pi^0$	$(-0.057, 0.046)$
$K_S^0\pi^-$	$(-0.025, 0.026)$
$K_S^0\pi^-\pi^0$	$(-0.062, 0.049)$
$K_S^0\pi^-\pi^-\pi^+$	$(-0.028, 0.027)$
$K^+K^-\pi^-$	$(-0.024, 0.023)$

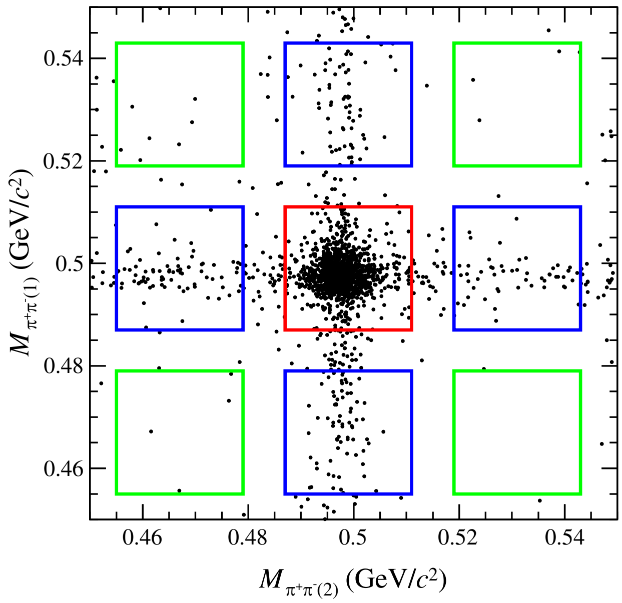

FIG. 2. Distribution of $M_{\pi^+\pi^-(1)}$ versus $M_{\pi^+\pi^-(2)}$ for the $D^+ \to K_S^0 K_S^0 \pi^+$ candidate events in data. The red solid box denotes the 2D signal region. The blue (green) solid boxes indicate the 2D sideband 1 (2) regions.

both $\pi^+\pi^-$ combinations lying in the one-dimensional (1D) K_S^0 signal region. The 2D K_S^0 sideband 1 (2) regions are defined as the square regions with 1 (2) $\pi^+\pi^-$ combination(s) located in the 1D K_S^0 sideband regions and the rest in the 1D K_S^0 signal region. Figure 2 shows the 2D distribution of $M_{\pi^+\pi^-(1)}$ versus $M_{\pi^+\pi^-(2)}$ for the $D^+ \to K_S^0 K_S^0 \pi^+$ candidates in data, where the two K_S^0 candidates are randomized.

In this analysis, the combinatorial background in the $M_{\pi^+\pi^-}$ distribution is assumed to be flat, and the net number of $D^+ \to K_S^0 K_S^0 \pi^+$ signal events is estimated as

$$N_{\rm net} = N_{K_S^0 {\rm sig}} - \frac{1}{2} N_{\rm sb1} + \frac{1}{4} N_{\rm sb2}, \qquad (2)$$

where $N_{K_S^0 {\rm sig}}$, $N_{\rm sb1}$, and $N_{\rm sb2}$ are the numbers of D^+ meson in the signal, the sideband 1, and the sideband 2 regions, respectively, from fitting the $M_{\rm BC}$ distributions of the accepted candidate events as explained in the next paragraph. The resulting $M_{\rm BC}$ distributions are shown in Fig. 3, and the measured value of $N_{\rm net}$ is given in Table III.

There are 1177 DT events obtained for the amplitude analysis with a signal purity of $(89.1 \pm 2.9)\%$, which is determined from a 2D unbinned maximum likelihood fit to the $M_{\rm BC}$ of the tag D^- versus the $M_{\rm BC}$ of the signal candidates. Figure 4 shows the $M_{\rm BC}^{\rm tag}$ versus $M_{\rm BC}^{\rm sig}$ distribution for the $D^+ \to K_S^0 K_S^0 \pi^+$ candidate events in data. The signal events with both the tag and the signal side correctly reconstructed concentrate around $M_{\rm BC}^{\rm sig} = M_{\rm BC}^{\rm tag} = m_{D^+}$, where m_{D^+} is the known D^+ mass. The resolution of the signal peak is primarily influenced by the momentum resolution of the detector and the beam energy spread. The $D^{+(-)}$ momentum resolution $\sigma(D^{+(-)})$ causes the signal peak to be smeared along the $M_{\rm BC}^{\rm sig}(M_{\rm BC}^{\rm tag})$ axis, while the beam energy spread $\sigma(E_{\rm beam})$ blurs the signal peak along the diagonal axis, $M_{\rm BC}^{\rm sig} + M_{\rm BC}^{\rm tag}$, due to its correlation with the $M_{\rm BC}^{\rm sig}$ and $M_{\rm BC}^{\rm tag}$ variables. Additionally, the signal peak is influenced by the ISR process, which makes the available $E_{\rm beam}$ smaller than the effective beam energy, leading to a diagonal ISR tail oriented toward the high diagonal axis. Besides signal events, we define three kinds of background. Candidates with correctly reconstructed D^+ (or D^-) and incorrectly reconstructed D^- (or D^+) are denoted as BG-I, which appear around the lines $M_{\rm BC}^{\rm sig}$ or $M_{\rm BC}^{\rm tag} = m_{D^+}$. Other candidates appearing along the diagonal (mispartitioning continuum) arise from decay modes sharing the same final state particle combination with the signal (BG-II). In these cases, one or more particles are associated with the wrong D meson, assuming all final state particles are well reconstructed. Consequently, the momentum of each signal or tag side is misreconstructed by the same amount, resulting in a corresponding shift in the $M_{\rm BC}$ of each side by the same amount. Moreover, some of the candidates smeared along the diagonal are from continuum events. The remaining background events mainly come from candidates reconstructed incorrectly on both sides (BG-III). Here we list the PDFs for the corresponding components [34,35] in the fit:

(i) Signal: $s(x, y)$,
(ii) BG-I: $b(x) \cdot c_y(y; E_{\rm beam}, \xi_y) + b(y) \cdot c_x(x; E_{\rm beam}, \xi_x)$,
(iii) BG-II: $c_z(z; \sqrt{2} E_{\rm beam}, \xi_z) \cdot g(k; 0, \sigma_k)$,
(iv) BG-III: $c_x(x; E_{\rm beam}, \xi_x) \cdot c_y(y; E_{\rm beam}, \xi_y)$.

Here, $x = M_{\rm BC}^{\rm tag}$, $y = M_{\rm BC}^{\rm sig}$, $z = (x + y)/\sqrt{2}$, and $k = (x - y)/\sqrt{2}$. The signal shape $s(x, y)$ is described by the 2D MC-simulated shape of D^+D^- convolved with two independent Gaussian functions. For BG-I, the function $b(x)$ is described by the 1D MC-simulated shape of $D^+(D^-)$ convolved with a Gaussian. The parameters of the Gaussian functions are obtained by a 1D fit to the $M_{\rm BC}$ distributions on the signal and tag side and are fixed in the 2D fit. The BG-II fit component is given by an ARGUS function in the diagonal axis multiplied by a Gaussian in the antidiagonal axis. The function $c_f(f; E_{\rm beam}, \xi_f)$ is the ARGUS function [36] defined as

$$c_f(f; E_{\rm beam}, \xi_f) = A_f f \left(1 - \frac{f^2}{E_{\rm beam}^2}\right)^{\frac{1}{2}} e^{\xi_f \left(1 - \frac{f^2}{E_{\rm beam}^2}\right)}, \qquad (3)$$

where f denotes x, y, or z, $E_{\rm beam}$ is fixed at 1.8865 GeV, A_f is a normalization factor, and ξ_f is a fit parameter. The function $g(k; \sigma_k)$ is a Gaussian distribution with a mean value of zero and a standard deviation $\sigma_k = \sigma_0 \cdot (\sqrt{2} E_{\rm beam} - z)^p$, where σ_0 and p are parameters determined by the fit. The BG-III fit component is given

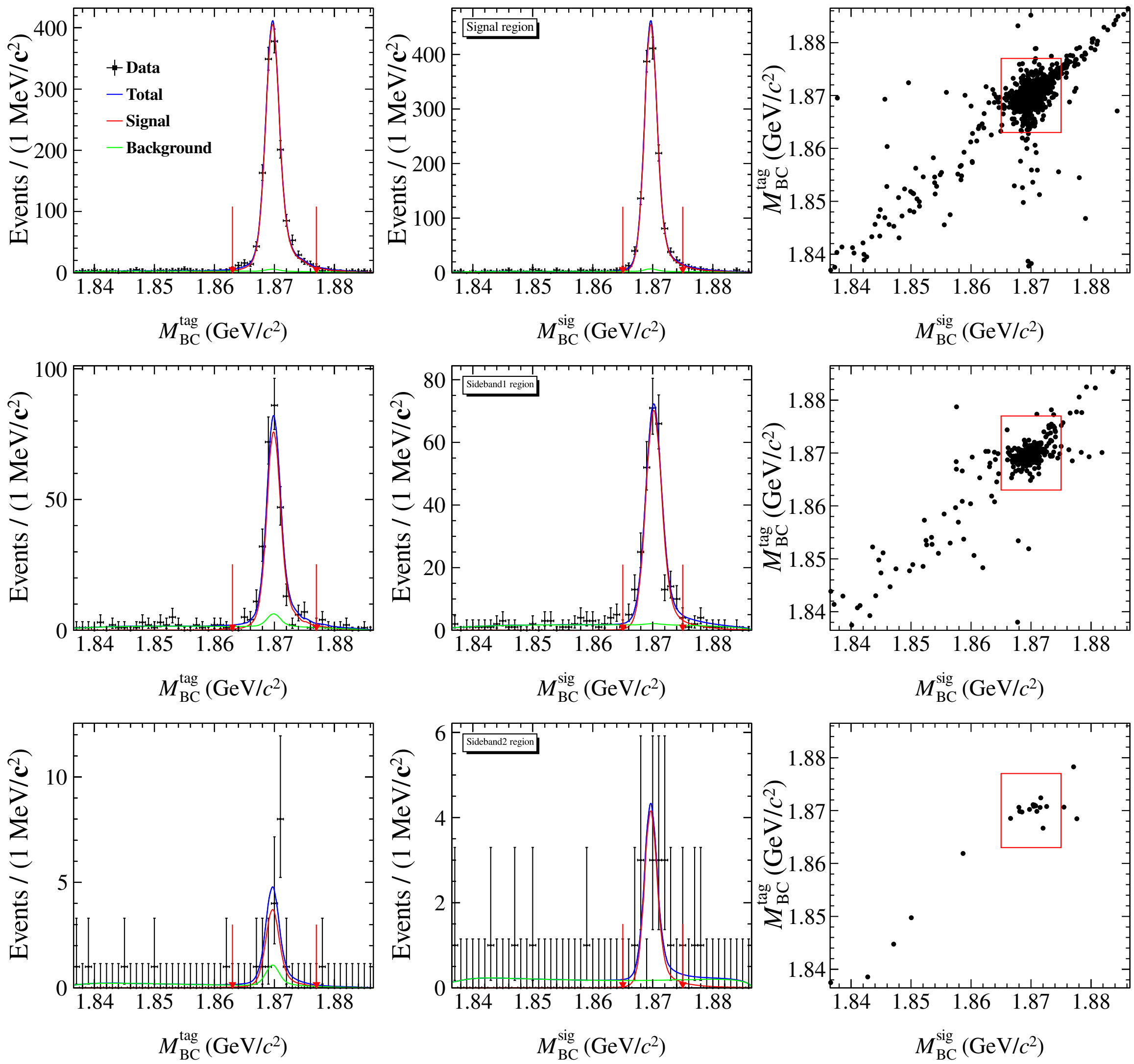

FIG. 3. Projections on $M_{\rm BC}^{\rm tag}$ (left) and $M_{\rm BC}^{\rm sig}$ (center) of the 2D fit. The black points with error bars are data, the blue lines are the total fit, the red lines are the signal shapes, the green lines are the sum of all backgrounds, and the pair of red arrows indicate the $M_{\rm BC}$ signal window. The right plots are the $M_{\rm BC}^{\rm tag}$ versus $M_{\rm BC}^{\rm sig}$ distributions, where the red box represents the signal region of $M_{\rm BC}$. The first, second, and third rows correspond to the fits to the candidate events in the signal, sideband 1, and sideband 2 regions, respectively.

by an ARGUS function in $M_{\rm BC}^{\rm sig}$ multiplied by an ARGUS function in $M_{\rm BC}^{\rm tag}$.

V. AMPLITUDE ANALYSIS

We perform a three-constraint kinematic fit to ensure that all the events lay within the phase space boundary, where the invariant masses of the signal D^+ and the two K_S^0 candidates are constrained to the corresponding known masses [29]. The updated four-momenta of the final state particles from the kinematic fit are used to perform the amplitude analysis. The amplitude analysis of $D^+ \to K_S^0 K_S^0 \pi^+$ is performed using an unbinned maximum likelihood fit. The likelihood function $\mathcal{L}$ is constructed as

$$\ln \mathcal{L} = \sum_k^{N_{\rm data}} \ln[\omega_{\rm sig} f_S(p_j^k) + (1-\omega_{\rm sig}) f_B(p_j^k)], \quad (4)$$

where k indicates the kth event in the data sample, $N_{\rm data}$ is the number of surviving events, p_j denotes the four-momenta of the jth final state particles, f_S (f_B) is the signal (background) PDF, and $\omega_{\rm sig}$ is the signal purity of the DT events.

TABLE III. Yields obtained from the 2D fit. The uncertainties are statistical only.

$N_{K_S^0 \rm sig}$	1296 ± 37
$N_{\rm sb1}$	244 ± 16
$N_{\rm sb2}$	11 ± 4
$N_{\rm net}$	1177 ± 38

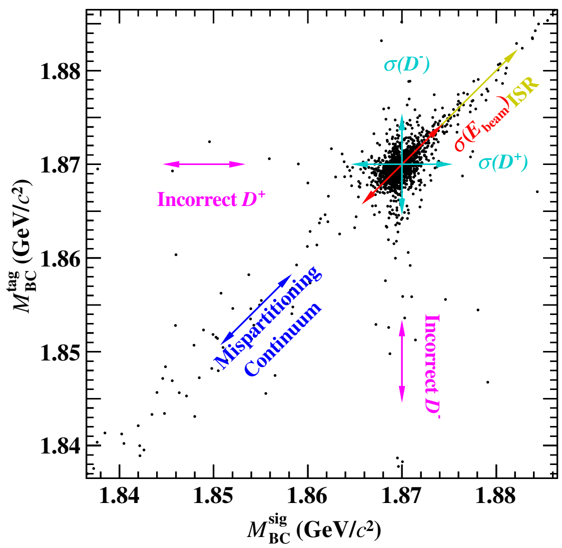

FIG. 4. Distribution of $M_{\rm BC}^{\rm tag}$ versus $M_{\rm BC}^{\rm sig}$ for the $D^+ \to K_S^0 K_S^0 \pi^+$ candidate events in data of K_S^0 signal region. The cyan arrows indicate the resolution caused by $D^{+(-)}$ momentum resolution ($\sigma(D^{+(-)})$), the red arrow by the beam energy spread ($\sigma(E_{\rm beam})$), and the yellow arrow denotes the ISR effect. The pink and blue arrows indicate the background due to incorrectly reconstructed D^- or D^+ and mispartitioning continuum, respectively.

The signal PDF is given by

$$f_S(p_j) = \frac{\epsilon(p_j)|\mathcal{M}(p_j)|^2 R_3(p_j)}{\int \epsilon(p_j)|\mathcal{M}(p_j)|^2 R_3(p_j)\mathrm{d}p_j}, \qquad (5)$$

where $\epsilon(p)$ is the detection efficiency and $R_3(p)$ is the three-body phase space. Based on the isobar model, the total amplitude $\mathcal{M}$ is constructed as the coherent sum of amplitudes of intermediate processes, given by $\mathcal{M}(p) = \sum c_n \mathcal{A}_n(p)$, where $c_n = \rho_n e^{i\phi_n}$ and $\mathcal{A}_n(p)$ are the complex coefficient and the amplitude for the nth intermediate process, respectively. The magnitude ρ_n and phase ϕ_n are free parameters in the fit. The model is symmetrized with respect to the two identical K_S^0 mesons. We use covariant tensors to construct the amplitudes, which are written as

$$\mathcal{A}_n = P_n S_n F_n^r F_n^D, \qquad (6)$$

where S_n is the spin factor [37], F_n^r and F_n^D are the Blatt-Weisskopf barrier factors of the intermediate state and the $D^\pm$ meson decays [38], respectively, and P_n is the relativistic Breit-Wigner (RBW) function [39] describing the propagator of the intermediate resonance. The background PDF is given by

$$f_B(p_j) = \frac{B(p_j)R_3(p_j)}{\int \epsilon(p_j)B_\epsilon(p_j)R_3(p_j)\mathrm{d}p_j}, \qquad (7)$$

where $B_\epsilon(p_j) = B(p_j)/\epsilon(p_j)$ is the efficiency-corrected background shape, and the $\epsilon(p_j)$ term is given by the number of selected events from the PHSP MC samples divided by the number of generated events in the $M^2_{K_S^0 K_S^0}$ versus $M^2_{K_S^0\pi^+}$ 2D space. The shape of the background in data is modeled by the background events in the signal region derived from the inclusive MC samples. The invariant mass distributions of events outside the signal region show good agreement between data and MC simulation, thus validating the description from the inclusive MC samples. We have also examined the distributions of the background events of the inclusive MC samples inside and outside the signal region. Generally, they are consistent with each other within statistical uncertainties. The background shape $B(p)$ is modeled using a kernel estimation method [40] implemented in ROOFIT [41] to model the distribution of an input dataset as a superposition of Gaussian kernels. The normalization integrals in the denominators are calculated by the phase space MC sample, which are

$$\int \epsilon|\mathcal{M}(p_j)|^2 R_3 \mathrm{d}p_j \propto \frac{1}{N_{\rm MC}} \sum_{k_{\rm MC}}^{N_{\rm MC}} \frac{|\mathcal{M}(p_j^{k_{\rm MC}})|^2}{|\mathcal{M}^{\rm gen}(p_j^{k_{\rm MC}})|^2}, \qquad (8)$$

$$\int \epsilon B_\epsilon(p_j) R_3 \mathrm{d}p_j \propto \frac{1}{N_{\rm MC}} \sum_{k_{\rm MC}}^{N_{\rm MC}} \frac{B_\epsilon(p_j^{k_{\rm MC}})}{|\mathcal{M}^{\rm gen}(p_j^{k_{\rm MC}})|^2}, \qquad (9)$$

where $k_{\rm MC}$ is the index of the kth event of the MC sample and $N_{\rm MC}$ is the number of selected MC events. The $\mathcal{M}^{\rm gen}(p_j)$ is the signal PDF used to generate the MC samples in MC integration.

Tracking, PID, and K_S^0 reconstruction efficiency differences between data and MC simulation are corrected by multiplying the MC events by a correction factor γ_ϵ, which is calculated as

$$\gamma_\epsilon(p_j) = \prod_n \frac{\epsilon_{n,\rm data}(p_j)}{\epsilon_{n,\rm MC}(p_j)}, \qquad (10)$$

where n refers to tracking, PID, or K_S^0 reconstruction, and $\epsilon_{n,\rm data}(p_j)$ and $\epsilon_{n,\rm MC}(p_j)$ are their efficiencies as a function of the momenta of the daughter particles for data and MC simulation, respectively. The specific values of these efficiencies are obtained using different control samples. More detailed information can be found in Sec. VII, as part of the uncertainty studies for the BF measurement. By weighting each MC event with γ_ϵ, the MC integration is modified to be

$$\int \epsilon|\mathcal{M}(p_j)|^2 R_3 \mathrm{d}p_j \propto \frac{1}{N_{\rm MC}} \sum_{k_{\rm MC}}^{N_{\rm MC}} \frac{\gamma_\epsilon |\mathcal{M}(p_j^{k_{\rm MC}})|^2}{|\mathcal{M}^{\rm gen}(p_j^{k_{\rm MC}})|^2}, \qquad (11)$$

$$\int \epsilon B_\epsilon R_3 \mathrm{d}p_j \propto \frac{1}{N_{\rm MC}} \sum_{k_{\rm MC}}^{N_{\rm MC}} \frac{\gamma_\epsilon B_\epsilon(p_j^{k_{\rm MC}})}{|\mathcal{M}^{\rm gen}(p_j^{k_{\rm MC}})|^2}. \qquad (12)$$

For a decay process $a \to bc$, the Blatt-Weisskopf barrier factors [38] depend on the angular momentum L and the momentum q of the final state particle b or c in the rest system of a. They are taken as

$$F_{L=0}(q) = 1,$$
$$F_{L=1}(q) = \sqrt{\frac{z_0^2+1}{z^2+1}},$$
$$F_{L=2}(q) = \sqrt{\frac{z_0^4+3z_0^2+9}{z^4+3z^2+9}}, \tag{13}$$

where $z = qR$ and $z_0 = q_0 R$. The effective radius of barrier R is fixed to be 3.0 $(\mathrm{GeV}/c)^{-1}$ for the intermediate resonances and 5.0 $(\mathrm{GeV}/c)^{-1}$ for the D^+ meson. The momentum q is given by

$$q = \sqrt{\frac{(s_a+s_b-s_c)^2}{4s_a} - s_b}, \tag{14}$$

where s_a, s_b, and s_c are the invariant mass squared of particles a, b, and c, respectively. The value of q_0 is that of q when $s_a = m_a^2$, where m_a is the mass of particle a.

The intermediate resonances $K^*(892)^+, K_2^*(1430)^+$, $f_0(1370)$, $a_0(1450)^0$, $K_0^*(1680)^+$ are parametrized with the RBW formulas,

$$P(m) = \frac{1}{m_0^2 - m^2 - i m_0 \Gamma(m)},$$
$$\Gamma(m) = \Gamma_0 \left(\frac{q}{q_0}\right)^{2L+1} \left(\frac{m_0}{m}\right) \left(\frac{F_L(q)}{F_L(q_0)}\right)^2, \tag{15}$$

where m is the invariant mass of the decay products, and m_0 and Γ_0 are the rest mass and width of the intermediate resonance, which are fixed to their known values [29]. The energy-dependent width is denoted by $\Gamma(m)$.

The $K\pi\mathcal{S}$-wave modeled by the LASS Collaboration [42] is described by a $K_0^*(1430)$ Breit-Wigner function together with an effective range nonresonant component with a phase shift, given by

$$A(m) = F \sin\delta_F e^{i\delta_F} + R \sin\delta_R e^{i\delta_R} e^{i2\delta_F}, \tag{16}$$

with

$$\delta_F = \phi_F + \cot^{-1}\left[\frac{1}{aq} + \frac{rq}{2}\right],$$
$$\delta_R = \phi_R + \tan^{-1}\left[\frac{M\Gamma(m_{K\pi})}{M^2 - m_{K\pi}^2}\right], \tag{17}$$

where the parameters $F(\phi_F)$ and $R(\phi_r)$ are the magnitudes (phases) for the nonresonant state and resonance terms, respectively. The parameters a and r are the scattering length and effective interaction length, respectively. M and Γ are the Breit-Wigner parameters of the $K_0^*(1430)$. We fix these parameters $(M, \Gamma, F, \phi_F, R, \phi_R, a, r)$ to the *BABAR* and Belle results [43]. These parameters are summarized in Table IV.

TABLE IV. The $K\pi\mathcal{S}$-wave parameters, obtained from the fit to the $D^0 \to K_S^0\pi^+\pi^-$ Dalitz plot distribution in the *BABAR* and Belle experiments [43]. Uncertainties are statistical only.

M (GeV/c^2)	1.441 ± 0.002
Γ (GeV)	0.193 ± 0.004
F	0.96 ± 0.07
$\phi_F(^\circ)$	0.1 ± 0.3
R	1 (fixed)
$\phi_R(^\circ)$	-109.7 ± 2.6
a (GeV/c^2)	0.113 ± 0.006
r (GeV/c^2)	-33.8 ± 1.8

The $f_0(980)$ is parametrized with the Flatté formula [44]

$$P_{f_0(980)} = \frac{1}{M_{f_0(980)}^2 - m^2 - i(g_{\pi\pi}\rho_{\pi\pi}(m^2) + g_{K\bar{K}}\rho_{K\bar{K}}(m^2))}, \tag{18}$$

where $g_{\pi\pi,K\bar{K}}$ are the coupling constants to individual final states. The parameters are fixed to be $g_{\pi\pi} = (0.165 \pm 0.010 \pm 0.015)\ \mathrm{GeV}^2/c^4$, $g_{K\bar{K}} = (4.21 \pm 0.25 \pm 0.21) g_{\pi\pi}$, and $M = 0.965\ \mathrm{GeV}/c^2$, as reported in Ref. [44]. The Lorentz invariant phase space factors $\rho_{\pi\pi}(s)$ and $\rho_{K\bar{K}}(s)$ are given by

$$\rho_{\pi\pi} = \frac{2}{3}\sqrt{1 - \frac{4m_{\pi^\pm}^2}{m^2}} + \frac{1}{3}\sqrt{1 - \frac{4m_{\pi^0}^2}{m^2}},$$
$$\rho_{K\bar{K}} = \frac{1}{2}\sqrt{1 - \frac{4m_{K^\pm}^2}{m^2}} + \frac{1}{2}\sqrt{1 - \frac{4m_{K^0}^2}{m^2}}. \tag{19}$$

Figure 5(a) shows the Dalitz plot of $M^2_{K_S^0(1)\pi^+}$ versus $M^2_{K_S^0(2)\pi^+}$ of the selected DT candidates from the data samples, where $K_S^0(1)$ and $K_S^0(2)$ are randomly selected from two indistinguishable K_S^0 candidates. The vertical and horizontal bands around 0.8 GeV^2/c^4 indicate the decay $D^+ \to K_S^0 K^*(892)^+$. We choose this process as a reference so that magnitudes and phases of other amplitudes are defined relative to it. Other possible contributions from the resonances such as $f_0(980)$, $f_0(1370)$, $K_2^*(1430)^+$, $a_0(1450)^0$, $K_0^*(1680)^+$, and $K\pi\,\mathcal{S}$-wave are added to the fit one at a time. The statistical significance of each resonance is calculated from the change of the log-likelihood taking the variation in the number of degrees of freedom into account. Different combinations of these resonances are

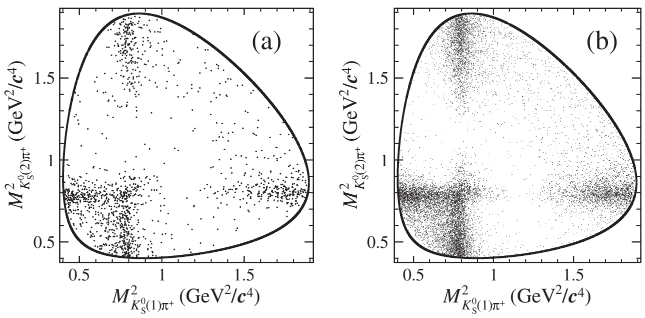

FIG. 5. Dalitz plots of $M^2_{K^0_S(1)\pi^+}$ versus $M^2_{K^0_S(2)\pi^+}$ for $D^+ \to K^0_S K^0_S \pi^+$, $K^0_S(1)$ and $K^0_S(2)$ are randomly selected from two indistinguishable K^0_S candidates, of (a) the sum of all data samples and (b) the signal MC samples generated based on the amplitude analysis result. The black curves indicate the kinematic boundary.

also tested. In addition to the reference amplitude $D^+ \to K^0_S K^*(892)^+$, the amplitude for $D^+ \to K^0_S(K^0_S\pi^+)_{\mathcal{S}\text{-wave}}$ is found to have a significance larger than 10σ. No other contribution has a significance larger than 3σ. The significance of the $f_0(980)$ contribution is less than 1σ. The Dalitz plot of the signal MC sample generated based on the result of the amplitude analysis is shown in Fig. 5(b). The mass projections of the fit are shown in Fig. 6. The fit quality is determined as $\chi^2/\mathrm{NDF} = 113.1/125$ using an adaptive binning of the $M^2_{K^0_S K^0_S}$ versus $M_{K^0_S\pi^+}$, where the Dalitz plot that each bin requires must contain at least ten events.

The contribution of the nth amplitude relative to the total BF is quantified by the fit fraction (FF) defined as $\mathrm{FF}_n = \int |\rho_n A_n|^2 dR_3 / \int |\mathcal{M}|^2 dR_3$. The FFs and the phase difference relative to the reference process are listed in Table V. The sum of the two FFs is 102.2%. The sum of these FFs is generally not unity due to net constructive or destructive interference.

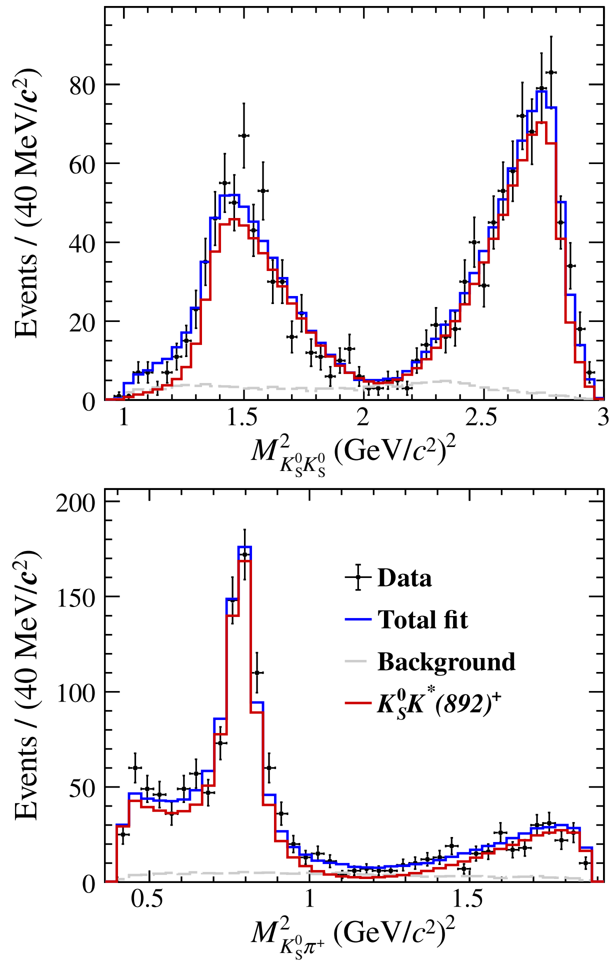

FIG. 6. Distributions of $M^2_{K^0_S K^0_S}$ and $M^2_{K^0_S\pi^+}$ from the nominal fit. The $M^2_{K^0_S\pi^+}$ distribution only contains one $K^0_S\pi^+$ combination, in which K^0_S is labeled randomly due to the indistinguishable K^0_S candidates. The points with error bars are data and the blue lines are the total fit result. The red solid lines are the $D^+ \to K^0_S K^*(892)^+$ component. The dashed gray lines are the simulated background derived from the inclusive MC sample.

VI. SYSTEMATIC UNCERTAINTY OF THE AMPLITUDE ANALYSIS

The systematic uncertainties for the amplitude analysis results, including the phase and FFs, can be categorized into the following sources: (I) input parameters, (II) radii of the mesons, (III) background, (IV) efficiency, (V) fit bias, (VI) insignificant amplitudes. For each kind of source, the related parameters are varied and the results of the new fit are compared to the results of the nominal fit, considering the difference as the corresponding uncertainty. The results of the systematic uncertainties for phase and FFs are summarized in Table VI, where the uncertainties are given in units of the corresponding statistical uncertainties. The total uncertainties are obtained by adding these contributions in quadrature.

(I) Input parameters: In the nominal fit, mass and width of the $K^*(892)^+$ are fixed to the values from PDG [29]. The parameters of the LASS model are fixed according to Ref. [43]. To estimate the corresponding systematic uncertainties, the fit procedure is repeated by varying one by one each of the fixed parameters by $\pm 1\sigma$. The quadratic sum of the largest relative variations for each parameter is taken as the systematic uncertainty.

(II) Radii of the mesons: The radii of the Blatt-Weisskopf barrier factors are varied from their nominal values of 5 and 3 GeV^{-1} (for the D^+ meson and the intermediate resonances, respectively) by ± 1 GeV^{-1}.

(III) Background: The uncertainties from the background size is studied by varying the signal fraction (equivalent to the fraction of background), i.e. ω_{sig} in Eq. (4), by $\pm 1\sigma$. Another source of systematic

TABLE V. The obtained FFs and phase difference to the reference amplitude. The first and the second uncertainties are statistical and systematic, respectively.

Amplitude	Phase	FF (%)
$D^+ \to K_S^0 K^*(892)^+$	0.0 (fixed)	$97.8 \pm 1.0 \pm 0.4$
$D^+ \to K_S^0 (K_S^0 \pi^+)_{\mathcal{S}-\rm wave}$	$1.4 \pm 0.2 \pm 0.1$	$4.4 \pm 1.0 \pm 0.5$

TABLE VI. Systematic uncertainties on the phase ϕ and FFs for different amplitudes in units of the corresponding statistical uncertainties. (I) input parameters, (II) radii of the mesons, (III) background, (IV) efficiency, (V) fit bias, (VI) insignificant amplitudes. The total systematic uncertainties are obtained by summing up all contributions in quadrature.

	$D^+ \to K_S^0 K^*(892)^+$	$D^+ \to K_S^0 (K_S^0 \pi^+)_{\mathcal{S}-\rm wave}$	
Source	FF	Phase ϕ	FF
I	0.12	0.15	0.06
II	0.12	0.14	0.06
III	0.13	0.12	0.10
IV	0.04	0.40	0.13
V	0.07	0.06	0.08
VI	0.34	0.38	0.43
Total	0.41	0.60	0.47

uncertainty comes from the modelization of the background shape, which is estimated by varying the parameter of RooNDKeysPDF describing the smoothness of the shape from 1.5 to 2 or 1, and extracting the shape with two different variables ($M^2_{K_S^0 K_S^0}$ and $M^2_{K_S^0 \pi^+}$). The largest difference from the nominal results is considered as the uncertainty.

(IV) Efficiency: The systematic uncertainty from the γ_ϵ factor in Eq. (10), which corrects for data-MC differences in tracking, PID and K_S^0 reconstruction efficiencies, is evaluated by performing the fit after varying the γ_ϵ factor by $\pm 1\sigma$.

Tracking and PID efficiencies of π^+ are studied by the control samples of $D^0 \to K^-\pi^+$, $D^0 \to K^-\pi^+\pi^0$, $D^0 \to K^-\pi^+\pi^+\pi^-$ versus $\bar{D}^0 \to K^+\pi^-$, $\bar{D}^0 \to K^+\pi^-\pi^0$, $\bar{D}^0 \to K^+\pi^-\pi^-\pi^+$, and $D^+ \to K^-\pi^+\pi^+$ versus $D^- \to K^+\pi^-\pi^-$. The K_S^0 reconstruction efficiency is studied by the control samples from $\psi(3770) \to D^0\bar{D}^0/D^+D^-$ and selected by DT method. The tag modes are $\bar{D}^0 \to K^-\pi^+$, $\bar{D}^0 \to K^-\pi^+\pi^0$, $\bar{D}^0 \to K^-\pi^+\pi^+\pi^-$, $D^- \to K^+\pi^-\pi^-$ and the signal modes are $D^0 \to K_S^0\pi^+\pi^-$, $D^0 \to K_S^0\pi^+\pi^-\pi^0$, $D^0 \to K_S^0\pi^0$, $D^+ \to K_S^0\pi^+$, $D^+ \to K_S^0\pi^+\pi^0$, $D^+ \to K_S^0\pi^+\pi^+\pi^-$.

(V) Fit bias: To tudy the possible bias from the fit procedure, an ensemble of 300 signal MC samples is generated according to the results of the amplitude analysis. The fit procedure is repeated for each signal MC sample, and the pull distributions of the amplitude results are fitted by a Gaussian. The obtained mean values are assigned as the correlated systematic uncertainties.

(VI) Insignificant amplitudes: The intermediate resonances with statistical significances less than 5σ are added to the model one by one. The largest variation from the nominal result is taken as the corresponding systematic uncertainty.

VII. BRANCHING FRACTION MEASUREMENT

The BF of $D^+ \to K_S^0 K_S^0 \pi^+$ is measured with the DT technique using the same tag modes and event selection criteria as the ones in the amplitude analysis. The BF is given by

$$\mathcal{B}_{\rm sig} = \frac{N_{\rm net}}{\sum_\alpha N_\alpha^{\rm ST} \epsilon_\alpha^{\rm DT} / \epsilon_\alpha^{\rm ST}}, \tag{20}$$

where α runs over the various tag modes. The DT efficiency ($\epsilon_\alpha^{\rm DT}$) is the signal selection efficiency for an event with a D^- in the αth tag mode. The ST yields ($N_\alpha^{\rm ST}$) and ST efficiencies ($\epsilon_\alpha^{\rm ST}$) for each tag mode are obtained by fitting the corresponding $M_{\rm BC}^{\rm tag}$ distributions individually. The corresponding $\epsilon_\alpha^{\rm DT}$, $N_\alpha^{\rm ST}$, and $\epsilon_\alpha^{\rm ST}$ are summarized in Table VII. The DT yield $N_{\rm net}$ is listed in Table III. In the fits to the $M_{\rm BC}^{\rm tag}$ distributions, the signal shape is modeled with the MC-simulated shape convolved with a double-Gaussian function. The background is parametrized as an ARGUS function [36] with an end point parameter fixed at $1.8865\ {\rm GeV}/c^2$. Figure 7 shows the fit results. The candidates with $M_{\rm BC}^{\rm tag}$ within $(1.863, 1.877)\ {\rm GeV}/c^2$ for each tag mode are kept for further analysis. The corresponding DT efficiencies $\epsilon_{\alpha,{\rm sig}}^{\rm DT}$ are obtained by analyzing the signal MC samples, with the signal events for $D^+ \to K_S^0 K_S^0 \pi^+$ generated based on the results of the amplitude analysis. After correcting for the differences in $\pi^\pm$ tracking, PID, and K_S^0 reconstruction efficiencies

TABLE VII. The ST yields ($N_\alpha^{\rm ST}$), ST efficiencies ($\epsilon_\alpha^{\rm ST}$), and DT efficiencies ($\epsilon_\alpha^{\rm DT}$) for six tag modes. The BFs of the subparticle (K_S^0, π^0) decays are not included. The uncertainties are statistical only.

Tag mode α	$N_\alpha^{\rm ST}$	$\epsilon_\alpha^{\rm ST}(\%)$	$\epsilon_\alpha^{\rm DT}(\%)$
$K^+\pi^-\pi^-$	2164074 ± 1571	51.17 ± 0.01	11.00 ± 0.01
$K^+\pi^-\pi^-\pi^0$	689042 ± 1172	25.50 ± 0.01	4.83 ± 0.01
$K_S^0\pi^-$	250437 ± 524	50.63 ± 0.02	10.83 ± 0.02
$K_S^0\pi^-\pi^0$	558495 ± 930	26.28 ± 0.01	4.98 ± 0.01
$K_S^0\pi^-\pi^-\pi^+$	300519 ± 669	28.97 ± 0.01	4.94 ± 0.01
$K^+K^-\pi^-$	187379 ± 541	41.06 ± 0.02	8.75 ± 0.02

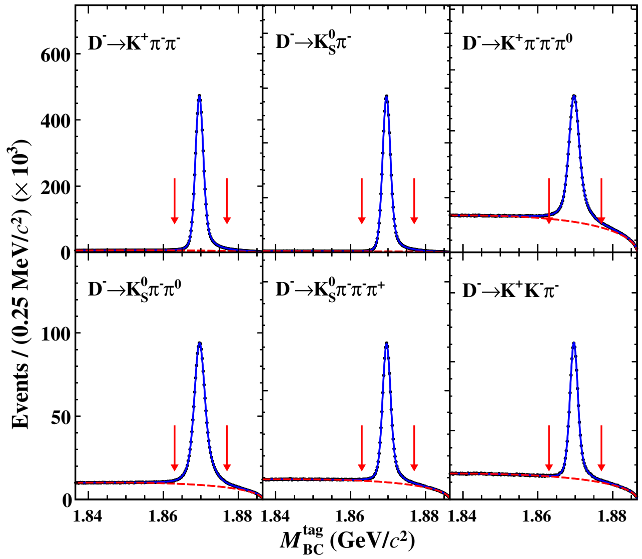

FIG. 7. Fits to the $M_{\mathrm{BC}}^{\mathrm{tag}}$ distributions of the ST D^- candidates. The data samples are represented by points with error bars, the total fit results by solid blue lines, and the red dashed curves describe the fitted combinatorial background shapes. The pair of red arrows indicate the M_{BC} signal window.

between data and MC simulation, we determine the BF to be $(2.97 \pm 0.09_{\mathrm{stat}} \pm 0.05_{\mathrm{syst}}) \times 10^{-3}$. The systematic uncertainty will be discussed in the following section.

VIII. SYSTEMATIC UNCERTAINTY OF BF MEASUREMENT

Most systematic uncertainties related to the efficiency of reconstructing the $D^\pm$ mesons on the tag side are canceled due to the DT method. The following sources are taken into consideration to evaluate the systematic uncertainties in the BF measurement. The total systematic uncertainties are summarized in Table VIII. Adding them in quadrature results in a total systematic uncertainty of 1.6% in the BF measurement.

(I) ST D^- yield: The systematic uncertainty in the ST yield has been estimated by varying the signal and background shapes in the fit. This systematic uncertainty is assigned to be 0.1%.

(II) Tracking and PID efficiencies: The data-MC efficiency ratios for π^- tracking and PID efficiencies are determined to be 0.998 ± 0.001 and 0.998 ± 0.001 for this decay channel by using the same control samples used for the amplitude analysis uncertainties. After correcting the MC efficiencies to data by these factors, the statistical uncertainties of the correction parameters are assigned as the systematic uncertainties, which are 0.1% for both $\pi^\pm$ PID and tracking.

(III) 2D fit: The uncertainty associated with the signal and background shapes in the 2D fit to the DT M_{BC} distribution is 1.1%, determined by varying the mean value and the resolution of the smeared Gaussian function by $\pm 1\sigma$ and varying the ARGUS end point by ± 0.2 MeV$/c^2$.

TABLE VIII. Systematic uncertainties for the BF measurement.

Source	Uncertainty (%)
ST D^- yield	0.1
PID efficiency	0.1
Tracking efficiency	0.1
2D fit	1.1
K_S^0 reconstruction	0.8
Amplitude model	0.2
Peaking background estimation	0.7
Quoted $\mathcal{B}$	0.1
ΔE requirement	0.5
Total	1.6

(IV) K_S^0 reconstruction: The data-MC efficiency ratio for K_S^0 reconstruction is determined to be 0.990 ± 0.004 by using the same control samples used for the amplitude analysis uncertainties. After correcting the efficiency by this factor for the two K_S^0 mesons, we assign 0.8% as the systematic uncertainty from the reconstruction of each K_S^0.

(V) Amplitude model: The uncertainty from the signal MC model based on the results of the amplitude analysis is studied by varying the fit parameters according to the covariance matrix. The change of signal efficiency is estimated to be 0.2%.

(VI) Peaking background estimation: According to Eq. (2), in the nominal analysis, the normalization factor for the peaking backgrounds (i.e. the ratio of the background yields between the K_S^0 signal and the sideband 1 regions) is assumed to be 0.5. The BF is recalculated with alternative normalization factors determined by MC simulation. The corresponding change on the BF, 0.7% for $D^+ \to K_S^0 K_S^0 \pi^+$, is assigned as the systematic uncertainty associated with the peaking background normalization. We have also examined the contributions of the sideband 2 region, but since the effects on the net number of events are negligible, we ignore them in this work.

(VII) Quoted $\mathcal{B}$: In this measurement, the BF of $K_S^0 \to \pi^+\pi^-$ is quoted from the PDG [29], which is $\mathcal{B}(K_S^0 \to \pi^+\pi^-) = (69.20 \pm 0.05)\%$. The associated uncertainty is assigned to be 0.1%.

(VIII) ΔE requirement: Considering the possible difference between data and MC simulation, we examine the ΔE_{sig} cut efficiency after smearing a double-Gaussian function for signal MC sample, and we take the change of this efficiency, 0.5%, as the systematic uncertainty.

IX. SUMMARY

Based on e^+e^- collision data corresponding to an integrated luminosity of $7.93\ \mathrm{fb}^{-1}$ collected with the BESIII detector at the center-of-mass energy 3.773 GeV, the first amplitude analysis of the decay $D^+ \to K_S^0 K_S^0 \pi^+$ is performed. The fit results are listed in Table V. In addition, with the detection efficiency obtained from the signal MC sample generated based on the amplitude analysis results, we obtain the BF $\mathcal{B}(D^+ \to K_S^0 K_S^0 \pi^+) = (2.97 \pm 0.09_{\mathrm{stat}} \pm 0.05_{\mathrm{syst}}) \times 10^{-3}$. The BF for $D^+ \to K_S^0 K^*(892)^+$ is calculated as $\mathrm{FF} \times \mathcal{B}(D^+ \to K_S^0 K_S^0 \pi^+)/\mathcal{B}(K^*(892)^+ \to K_S^0 \pi^+)$ to be $\mathcal{B}(D^+ \to K_S^0 K^*(892)^+) = (8.72 \pm 0.28_{\mathrm{stat}} \pm 0.15_{\mathrm{syst}}) \times 10^{-3}$, which is consistent with the previous BESIII measurement [11] but with improved precision.

Compared to the theoretical expectations of Table I, this result deviates from those in Refs. [2,13] by more than 5 standard deviations, while it is consistent with that based on the theoretical expectations [12,14] within 2 standard deviations and the predictions in Ref. [1] within 3 standard deviations.

ACKNOWLEDGMENTS

The BESIII Collaboration thanks the staff of BEPCII and the IHEP computing center for their strong support. This work is supported in part by National Key R&D Program of China under Contracts No. 2023YFA1606000, No. 2020YFA0406400, No. 2020YFA0406300; National Natural Science Foundation of China (NSFC) under Contracts No. 11635010, No. 11735014, No. 11935015, No. 11935016, No. 11935018, No. 12025502, No. 12035009, No. 12035013, No. 12061131003, No. 12192260, No. 12192261, No. 12192262, No. 12192263, No. 12192264, No. 12192265, No. 12221005, No. 12225509, No. 12235017, No. 12361141819, No. 12375087, No. 18175054; the Chinese Academy of Sciences (CAS) Large-Scale Scientific Facility Program; the CAS Center for Excellence in Particle Physics (CCEPP); Joint Large-Scale Scientific Facility Funds of the NSFC and CAS under Contracts No. U1832207, No. U2032104; the Excellent Youth Foundation of Henan Scientific Committee under Contract No. 242300421044; 100 Talents Program of CAS; The Institute of Nuclear and Particle Physics (INPAC) and Shanghai Key Laboratory for Particle Physics and Cosmology; German Research Foundation DFG under Contracts No. 455635585, No. FOR5327, No. GRK 2149; Istituto Nazionale di Fisica Nucleare, Italy; Ministry of Development of Turkey under Contract No. DPT2006K-120470; National Research Foundation of Korea under Contract No. NRF-2022R1A2C1092335; National Science and Technology fund of Mongolia; National Science Research and Innovation Fund (NSRF) via the Program Management Unit for Human Resources and Institutional Development, Research and Innovation of Thailand under Contract No. B16F640076; Polish National Science Centre under Contract No. 2019/35/O/ST2/02907; The Swedish Research Council; U.S. Department of Energy under Contract No. DE-FG02-05ER41374.

[1] H. Y. Cheng, C. W. Chiang, and A. L. Kuo, Phys. Rev. D **93**, 114010 (2016).
[2] H. Y. Cheng and C. W. Chiang, Phys. Rev. D **100**, 093002 (2019).
[3] H. Y. Cheng and C. W. Chiang, Phys. Rev. D **81**, 074021 (2010).
[4] X. H. Zhang, H. Zhang, B. C. Ke, L. J. Liu, D. M. Li, and E. Wang, arXiv:2409.09966.
[5] M. Y. Duan, J. Y. Wang, G. Y. Wang, E. Wang, and D. M. Li, Eur. Phys. J. C **80**, 1041 (2020).
[6] Y. K. Hsiao, Y. Yu, and B. C. Ke, Eur. Phys. J. C **80**, 895 (2020).
[7] Y. Yu, Y. K. Hsiao, and B. C. Ke, Eur. Phys. J. C **81**, 1093 (2021).
[8] Y. K. Hsiao, S. Q. Yang, W. J. Wei, and B. C. Ke, arXiv:2306.06091.
[9] Y. Cao, Y. Cheng, and Q. Zhao, Phys. Rev. D **109**, 073002 (2024).
[10] M. Ablikim *et al.* (BESIII Collaboration), Phys. Rev. D **99**, 032002 (2019).
[11] M. Ablikim *et al.* (BESIII Collaboration), Phys. Rev. D **104**, 012006 (2021).
[12] F. S. Yu, X. X. Wang, and C. D. Lyu, Phys. Rev. D **84**, 074019 (2011).
[13] Q. Qin, H. N. Li, C. D. Lyu, and F. S. Yu, Phys. Rev. D **89**, 054006 (2014).
[14] H. Y. Cheng and C. W. Chiang, Phys. Rev. D **109**, 073008 (2024).
[15] M. Ablikim *et al.* (BESIII Collaboration), Phys. Lett. B **765**, 231 (2017).
[16] M. Ablikim *et al.* (BESIII Collaboration), Chin. Phys. C **37**, 123001 (2013).
[17] M. Ablikim *et al.* (BESIII Collaboration), Phys. Lett. B **753**, 629 (2016).
[18] M. Ablikim *et al.* (BESIII Collaboration), Chin. Phys. C **48**, 123001 (2024).
[19] M. Ablikim *et al.* (BESIII Collaboration), Nucl. Instrum. Methods Phys. Res., Sect. A **614**, 345 (2010).
[20] C. H. Yu *et al.*, Proceedings of IPAC2016, Busan, Korea (2016), http://jacow.org/ipac2016/papers/tuya01.pdf.

[21] M. Ablikim *et al.* (BESIII Collaboration), Chin. Phys. C **44**, 040001 (2020).
[22] J. Lu, Y. Xiao, and X. Ji, Radiat. Detect. Technol. Methods **4**, 337 (2020).
[23] J. W. Zhang *et al.*, Radiat. Detect. Technol. Methods **6**, 289 (2022).
[24] X. Li *et al.*, Radiat. Detect. Technol. Methods **1**, 13 (2017); Y. X. Guo *et al.*, Radiat. Detect. Technol. Methods **1**, 15 (2017); P. Cao *et al.*, Nucl. Instrum. Methods Phys. Res., Sect. A **953**, 163053 (2020).
[25] S. Agostinelli *et al.* (GEANT4 Collaboration), Nucl. Instrum. Methods Phys. Res., Sect. A **506**, 250 (2003).
[26] K. X. Huang *et al.*, Nucl. Sci. Tech. **33**, 142 (2022).
[27] S. Jadach, B. F. L. Ward, and Z. Was, Phys. Rev. D **63**, 113009 (2001); Comput. Phys. Commun. **130**, 260 (2000).
[28] D. J. Lange, Nucl. Instrum. Methods Phys. Res., Sect. A **462**, 152 (2001); R. G. Ping, Chin. Phys. C **32**, 599 (2008).
[29] R. L. Workman *et al.* (Particle Data Group), Prog. Theor. Exp. Phys. **2022**, 083C01 (2022).
[30] J. C. Chen, G. S. Huang, X. R. Qi, D. H. Zhang, and Y. S. Zhu, Phys. Rev. D **62**, 034003 (2000); R. L. Yang, R. G. Ping, and H. Chen, Chin. Phys. Lett. **31**, 061301 (2014).
[31] E. Richter-Was, Phys. Lett. B **303**, 163 (1993).
[32] J. Adler *et al.* (MARK-III Collaboration), Phys. Rev. Lett. **62**, 1821 (1989).
[33] B. C. Ke, J. Koponen, H. B. Li, and Y. Zheng, Annu. Rev. Nucl. Part. Sci. **73**, 285–314 (2023).
[34] M. Ablikim *et al.* (BESIII Collaboration), Phys. Rev. D **101**, 052009 (2020).
[35] M. Artuso *et al.* (CLEO Collaboration), Phys. Rev. D **76**, 112001 (2007).
[36] H. Albrecht *et al.* (ARGUS Collaboration), Phys. Lett. B **241**, 278 (1990).
[37] B. S. Zou and D. V. Bugg, Eur. Phys. J. A **16**, 537 (2003).
[38] J. M. Blatt and V. F. Weisskopf, *Theoretical Nuclear Physics* (John Wiley & Sons, New York, 1973).
[39] J. D. Jackson, Nuovo Cimento **34**, 1644 (1964).
[40] K. Cranmer, Comput. Phys. Commun. **136**, 198 (2001).
[41] W. Verkerke and D. P. Kirkby, RooFit Users Manual v2.91 (2019), http://roofit.sourceforge.net.
[42] D. Aston *et al.*, Nucl. Phys. **B296**, 493 (1988).
[43] I. Adachi *et al.* (*BABAR* and Belle Collaborations), Phys. Rev. D **98**, 112012 (2018).
[44] M. Ablikim *et al.* (BESIII Collaboration), Phys. Lett. B **607**, 243 (2005).

M. Ablikim,[1] M. N. Achasov,[4,c] P. Adlarson,[76] O. Afedulidis,[3] X. C. Ai,[81] R. Aliberti,[35] A. Amoroso,[75a,75c] Q. An,[72,58,a] Y. Bai,[57] O. Bakina,[36] I. Balossino,[29a] Y. Ban,[46,h] H.-R. Bao,[64] V. Batozskaya,[1,44] K. Begzsuren,[32] N. Berger,[35] M. Berlowski,[44] M. Bertani,[28a] D. Bettoni,[29a] F. Bianchi,[75a,75c] E. Bianco,[75a,75c] A. Bortone,[75a,75c] I. Boyko,[36] R. A. Briere,[5] A. Brueggemann,[69] H. Cai,[77] X. Cai,[1,58] A. Calcaterra,[28a] G. F. Cao,[1,64] N. Cao,[1,64] S. A. Cetin,[62a] J. F. Chang,[1,58] G. R. Che,[43] G. Chelkov,[36,b] C. Chen,[43] C. H. Chen,[9] Chao Chen,[55] G. Chen,[1] H. S. Chen,[1,64] H. Y. Chen,[20] M. L. Chen,[1,58,64] S. J. Chen,[42] S. L. Chen,[45] S. M. Chen,[61] T. Chen,[1,64] X. R. Chen,[31,64] X. T. Chen,[1,64] Y. B. Chen,[1,58] Y. Q. Chen,[34] Z. J. Chen,[25,i] Z. Y. Chen,[1,64] S. K. Choi,[10] G. Cibinetto,[29a] F. Cossio,[75c] J. J. Cui,[50] H. L. Dai,[1,58] J. P. Dai,[79] A. Dbeyssi,[18] R. E. de Boer,[3] D. Dedovich,[36] C. Q. Deng,[73] Z. Y. Deng,[1] A. Denig,[35] I. Denysenko,[36] M. Destefanis,[75a,75c] F. De Mori,[75a,75c] B. Ding,[67,1] X. X. Ding,[46,h] Y. Ding,[40] Y. Ding,[34] J. Dong,[1,58] L. Y. Dong,[1,64] M. Y. Dong,[1,58,64] X. Dong,[77] M. C. Du,[1] S. X. Du,[81] Y. Y. Duan,[55] Z. H. Duan,[42] P. Egorov,[36,b] Y. H. Fan,[45] J. Fang,[1,58] J. Fang,[59] S. S. Fang,[1,64] W. X. Fang,[1] Y. Fang,[1] Y. Q. Fang,[1,58] R. Farinelli,[29a] L. Fava,[75b,75c] F. Feldbauer,[3] G. Felici,[28a] C. Q. Feng,[72,58] J. H. Feng,[59] Y. T. Feng,[72,58] M. Fritsch,[3] C. D. Fu,[1] J. L. Fu,[64] Y. W. Fu,[1,64] H. Gao,[64] X. B. Gao,[41] Y. N. Gao,[46,h] Yang Gao,[72,58] S. Garbolino,[75c] I. Garzia,[29a,29b] L. Ge,[81] P. T. Ge,[19] Z. W. Ge,[42] C. Geng,[59] E. M. Gersabeck,[68] A. Gilman,[70] K. Goetzen,[13] L. Gong,[40] W. X. Gong,[1,58] W. Gradl,[35] S. Gramigna,[29a,29b] M. Greco,[75a,75c] M. H. Gu,[1,58] Y. T. Gu,[15] C. Y. Guan,[1,64] A. Q. Guo,[31,64] L. B. Guo,[41] M. J. Guo,[50] R. P. Guo,[49] Y. P. Guo,[12,g] A. Guskov,[36,b] J. Gutierrez,[27] K. L. Han,[64] T. T. Han,[1] F. Hanisch,[3] X. Q. Hao,[19] F. A. Harris,[66] K. K. He,[55] K. L. He,[1,64] F. H. Heinsius,[3] C. H. Heinz,[35] Y. K. Heng,[1,58,64] C. Herold,[60] T. Holtmann,[3] P. C. Hong,[34] G. Y. Hou,[1,64] X. T. Hou,[1,64] Y. R. Hou,[64] Z. L. Hou,[1] B. Y. Hu,[59] H. M. Hu,[1,64] J. F. Hu,[56,j] S. L. Hu,[12,g] T. Hu,[1,58,64] Y. Hu,[1] G. S. Huang,[72,58] K. X. Huang,[59] L. Q. Huang,[31,64] X. T. Huang,[50] Y. P. Huang,[1] Y. S. Huang,[59] T. Hussain,[74] F. Hölzken,[3] N. Hüsken,[35] N. in der Wiesche,[69] J. Jackson,[27] S. Janchiv,[32] J. H. Jeong,[10] Q. Ji,[1] Q. P. Ji,[19] W. Ji,[1,64] X. B. Ji,[1,64] X. L. Ji,[1,58] Y. Y. Ji,[50] X. Q. Jia,[50] Z. K. Jia,[72,58] D. Jiang,[1,64] H. B. Jiang,[77] P. C. Jiang,[46,h] S. S. Jiang,[39] T. J. Jiang,[16] X. S. Jiang,[1,58,64] Y. Jiang,[64] J. B. Jiao,[50] J. K. Jiao,[34] Z. Jiao,[23] S. Jin,[42] Y. Jin,[67] M. Q. Jing,[1,64] X. M. Jing,[64] T. Johansson,[76] S. Kabana,[33] N. Kalantar-Nayestanaki,[65] X. L. Kang,[9] X. S. Kang,[40] M. Kavatsyuk,[65] B. C. Ke,[81] V. Khachatryan,[27] A. Khoukaz,[69] R. Kiuchi,[1] O. B. Kolcu,[62a] B. Kopf,[3] M. Kuessner,[3] X. Kui,[1,64] N. Kumar,[26] A. Kupsc,[44,76] W. Kühn,[37] J. J. Lane,[68] L. Lavezzi,[75a,75c] T. T. Lei,[72,58] Z. H. Lei,[72,58] M. Lellmann,[35] T. Lenz,[35] C. Li,[47] C. Li,[43] C. H. Li,[39] Cheng Li,[72,58] D. M. Li,[81] F. Li,[1,58] G. Li,[1] H. B. Li,[1,64] H. J. Li,[19] H. N. Li,[56,j] Hui Li,[43] J. R. Li,[61]

J. S. Li,[59] K. Li,[1] L. J. Li,[1,64] L. K. Li,[1] Lei Li,[48] M. H. Li,[43] P. R. Li,[38,k,l] Q. M. Li,[1,64] Q. X. Li,[50] R. Li,[17,31] S. X. Li,[12] T. Li,[50] W. D. Li,[1,64] W. G. Li,[1,a] X. Li,[1,64] X. H. Li,[72,58] X. L. Li,[50] X. Y. Li,[1,64] X. Z. Li,[59] Y. G. Li,[46,h] Z. J. Li,[59] Z. Y. Li,[79] C. Liang,[42] H. Liang,[72,58] H. Liang,[1,64] Y. F. Liang,[54] Y. T. Liang,[31,64] G. R. Liao,[14] Y. P. Liao,[1,64] J. Libby,[26] A. Limphirat,[60] C. C. Lin,[55] D. X. Lin,[31,64] T. Lin,[1] B. J. Liu,[1] B. X. Liu,[77] C. Liu,[34] C. X. Liu,[1] F. Liu,[1] F. H. Liu,[53] Feng Liu,[6] G. M. Liu,[56,j] H. Liu,[38,k,l] H. B. Liu,[15] H. H. Liu,[1] H. M. Liu,[1,64] Huihui Liu,[21] J. B. Liu,[72,58] J. Y. Liu,[1,64] K. Liu,[38,k,l] K. Y. Liu,[40] Ke Liu,[22] L. Liu,[72,58] L. C. Liu,[43] Lu Liu,[43] M. H. Liu,[12,g] P. L. Liu,[1] Q. Liu,[64] S. B. Liu,[72,58] T. Liu,[12,g] W. K. Liu,[43] W. M. Liu,[72,58] X. Liu,[39] X. Liu,[38,k,l] Y. Liu,[81] Y. Liu,[38,k,l] Y. B. Liu,[43] Z. A. Liu,[1,58,64] Z. D. Liu,[9] Z. Q. Liu,[50] X. C. Lou,[1,58,64] F. X. Lu,[59] H. J. Lu,[23] J. G. Lu,[1,58] X. L. Lu,[1] Y. Lu,[7] Y. P. Lu,[1,58] Z. H. Lu,[1,64] C. L. Luo,[41] J. R. Luo,[59] M. X. Luo,[80] T. Luo,[12,g] X. L. Luo,[1,58] X. R. Lyu,[64] Y. F. Lyu,[43] F. C. Ma,[40] H. Ma,[79] H. L. Ma,[1] J. L. Ma,[1,64] L. L. Ma,[50] L. R. Ma,[67] M. M. Ma,[1,64] Q. M. Ma,[1] R. Q. Ma,[1,64] T. Ma,[72,58] X. T. Ma,[1,64] X. Y. Ma,[1,58] Y. Ma,[46,h] Y. M. Ma,[31] F. E. Maas,[18] M. Maggiora,[75a,75c] S. Malde,[70] Y. J. Mao,[46,h] Z. P. Mao,[1] S. Marcello,[75a,75c] Z. X. Meng,[67] J. G. Messchendorp,[13,65] G. Mezzadri,[29a] H. Miao,[1,64] T. J. Min,[42] R. E. Mitchell,[27] X. H. Mo,[1,58,64] B. Moses,[27] N. Yu. Muchnoi,[4,c] J. Muskalla,[35] Y. Nefedov,[36] F. Nerling,[18,e] L. S. Nie,[20] I. B. Nikolaev,[4,c] Z. Ning,[1,58] S. Nisar,[11,m] Q. L. Niu,[38,k,l] W. D. Niu,[55] Y. Niu,[50] S. L. Olsen,[64] Q. Ouyang,[1,58,64] S. Pacetti,[28b,28c] X. Pan,[55] Y. Pan,[57] A. Pathak,[34] Y. P. Pei,[72,58] M. Pelizaeus,[3] H. P. Peng,[72,58] Y. Y. Peng,[38,k,l] K. Peters,[13,e] J. L. Ping,[41] R. G. Ping,[1,64] S. Plura,[35] V. Prasad,[33] F. Z. Qi,[1] H. Qi,[72,58] H. R. Qi,[61] M. Qi,[42] T. Y. Qi,[12,g] S. Qian,[1,58] W. B. Qian,[64] C. F. Qiao,[64] X. K. Qiao,[81] J. J. Qin,[73] L. Q. Qin,[14] L. Y. Qin,[72,58] X. P. Qin,[12,g] X. S. Qin,[50] Z. H. Qin,[1,58] J. F. Qiu,[1] Z. H. Qu,[73] C. F. Redmer,[35] K. J. Ren,[39] A. Rivetti,[75c] M. Rolo,[75c] G. Rong,[1,64] Ch. Rosner,[18] S. N. Ruan,[43] N. Salone,[44] A. Sarantsev,[36,d] Y. Schelhaas,[35] K. Schoenning,[76] M. Scodeggio,[29a] K. Y. Shan,[12,g] W. Shan,[24] X. Y. Shan,[72,58] Z. J. Shang,[38,k,l] J. F. Shangguan,[16] L. G. Shao,[1,64] M. Shao,[72,58] C. P. Shen,[12,g] H. F. Shen,[1,8] W. H. Shen,[64] X. Y. Shen,[1,64] B. A. Shi,[64] H. Shi,[72,58] H. C. Shi,[72,58] J. L. Shi,[12,g] J. Y. Shi,[1] Q. Q. Shi,[55] S. Y. Shi,[73] X. Shi,[1,58] J. J. Song,[19] T. Z. Song,[59] W. M. Song,[34,1] Y. J. Song,[12,g] Y. X. Song,[46,h,n] S. Sosio,[75a,75c] S. Spataro,[75a,75c] F. Stieler,[35] Y. J. Su,[64] G. B. Sun,[77] G. X. Sun,[1] H. Sun,[64] H. K. Sun,[1] J. F. Sun,[19] K. Sun,[61] L. Sun,[77] S. S. Sun,[1,64] T. Sun,[51,f] W. Y. Sun,[34] Y. Sun,[9] Y. J. Sun,[72,58] Y. Z. Sun,[1] Z. Q. Sun,[1,64] Z. T. Sun,[50] C. J. Tang,[54] G. Y. Tang,[1] J. Tang,[59] M. Tang,[72,58] Y. A. Tang,[77] L. Y. Tao,[73] Q. T. Tao,[25,i] M. Tat,[70] J. X. Teng,[72,58] V. Thoren,[76] W. H. Tian,[59] Y. Tian,[31,64] Z. F. Tian,[77] I. Uman,[62b] Y. Wan,[55] S. J. Wang,[50] B. Wang,[1] B. L. Wang,[64] Bo Wang,[72,58] D. Y. Wang,[46,h] F. Wang,[73] H. J. Wang,[38,k,l] J. J. Wang,[77] J. P. Wang,[50] K. Wang,[1,58] L. L. Wang,[1] M. Wang,[50] N. Y. Wang,[64] S. Wang,[12,g] S. Wang,[38,k,l] T. Wang,[12,g] T. J. Wang,[43] W. Wang,[73] W. Wang,[59] W. P. Wang,[35,72,o] W. P. Wang,[72,58] X. Wang,[46,h] X. F. Wang,[38,k,l] X. J. Wang,[39] X. L. Wang,[12,g] X. N. Wang,[1] Y. Wang,[61] Y. D. Wang,[45] Y. F. Wang,[1,58,64] Y. L. Wang,[19] Y. N. Wang,[45] Y. Q. Wang,[1] Yaqian Wang,[17] Yi Wang,[61] Z. Wang,[1,58] Z. L. Wang,[73] Z. Y. Wang,[1,64] Ziyi Wang,[64] D. H. Wei,[14] F. Weidner,[69] S. P. Wen,[1] Y. R. Wen,[39] U. Wiedner,[3] G. Wilkinson,[70] M. Wolke,[76] L. Wollenberg,[3] C. Wu,[39] J. F. Wu,[1,8] L. H. Wu,[1] L. J. Wu,[1,64] X. Wu,[12,g] X. H. Wu,[34] Y. Wu,[72,58] Y. H. Wu,[55] Y. J. Wu,[31] Z. Wu,[1,58] L. Xia,[72,58] X. M. Xian,[39] B. H. Xiang,[1,64] T. Xiang,[46,h] D. Xiao,[38,k,l] G. Y. Xiao,[42] S. Y. Xiao,[1] Y. L. Xiao,[12,g] Z. J. Xiao,[41] C. Xie,[42] X. H. Xie,[46,h] Y. Xie,[50] Y. G. Xie,[1,58] Y. H. Xie,[6] Z. P. Xie,[72,58] T. Y. Xing,[1,64] C. F. Xu,[1,64] C. J. Xu,[59] G. F. Xu,[1] H. Y. Xu,[67,2,p] M. Xu,[72,58] Q. J. Xu,[16] Q. N. Xu,[30] W. Xu,[1] W. L. Xu,[67] X. P. Xu,[55] Y. C. Xu,[78] Z. S. Xu,[64] F. Yan,[12,g] L. Yan,[12,g] W. B. Yan,[72,58] W. C. Yan,[81] X. Q. Yan,[1,64] H. J. Yang,[51,f] H. L. Yang,[34] H. X. Yang,[1] T. Yang,[1] Y. Yang,[12,g] Y. F. Yang,[1,64] Y. F. Yang,[43] Y. X. Yang,[1,64] Z. W. Yang,[38,k,l] Z. P. Yao,[50] M. Ye,[1,58] M. H. Ye,[8] J. H. Yin,[1] Junhao Yin,[43] Z. Y. You,[59] B. X. Yu,[1,58,64] C. X. Yu,[43] G. Yu,[1,64] J. S. Yu,[25,i] T. Yu,[73] X. D. Yu,[46,h] Y. C. Yu,[81] C. Z. Yuan,[1,64] J. Yuan,[45] J. Yuan,[34] L. Yuan,[2] S. C. Yuan,[1,64] Y. Yuan,[1,64] Z. Y. Yuan,[59] C. X. Yue,[39] A. A. Zafar,[74] F. R. Zeng,[50] S. H. Zeng,[63] X. Zeng,[12,g] Y. Zeng,[25,i] Y. J. Zeng,[59] Y. J. Zeng,[1,64] X. Y. Zhai,[34] Y. C. Zhai,[50] Y. H. Zhan,[59] A. Q. Zhang,[1,64] B. L. Zhang,[1,64] B. X. Zhang,[1] D. H. Zhang,[43] G. Y. Zhang,[19] H. Zhang,[81] H. Zhang,[72,58] H. C. Zhang,[1,58,64] H. H. Zhang,[59] H. H. Zhang,[34] H. Q. Zhang,[1,58,64] H. R. Zhang,[72,58] H. Y. Zhang,[1,58] J. Zhang,[81] J. Zhang,[59] J. J. Zhang,[52] J. L. Zhang,[20] J. Q. Zhang,[41] J. S. Zhang,[12,g] J. W. Zhang,[1,58,64] J. X. Zhang,[38,k,l] J. Y. Zhang,[1] J. Z. Zhang,[1,64] Jianyu Zhang,[64] L. M. Zhang,[61] Lei Zhang,[42] P. Zhang,[1,64] Q. Y. Zhang,[34] R. Y. Zhang,[38,k,l] S. H. Zhang,[1,64] Shulei Zhang,[25,i] X. D. Zhang,[45] X. M. Zhang,[1] X. Y. Zhang,[50] Y. Zhang,[73] Y. Zhang,[1] Y. T. Zhang,[81] Y. H. Zhang,[1,58] Y. M. Zhang,[39] Yan Zhang,[72,58] Z. D. Zhang,[1] Z. H. Zhang,[1] Z. L. Zhang,[34] Z. Y. Zhang,[43] Z. Y. Zhang,[77] Z. Z. Zhang,[45] G. Zhao,[1] J. Y. Zhao,[1,64] J. Z. Zhao,[1,58] L. Zhao,[1] Lei Zhao,[72,58] M. G. Zhao,[43] N. Zhao,[79] R. P. Zhao,[64] S. J. Zhao,[81] Y. B. Zhao,[1,58] Y. X. Zhao,[31,64] Z. G. Zhao,[72,58] A. Zhemchugov,[36,b] B. Zheng,[73] B. M. Zheng,[34] J. P. Zheng,[1,58] W. J. Zheng,[1,64] Y. H. Zheng,[64] B. Zhong,[41] X. Zhong,[59] H. Zhou,[50] J. Y. Zhou,[34] L. P. Zhou,[1,64] S. Zhou,[6] X. Zhou,[77]

X. K. Zhou,[6] X. R. Zhou,[72,58] X. Y. Zhou,[39] Y. Z. Zhou,[12,g] A. N. Zhu,[64] J. Zhu,[43] K. Zhu,[1] K. J. Zhu,[1,58,64] K. S. Zhu,[12,g] L. Zhu,[34] L. X. Zhu,[64] S. H. Zhu,[71] T. J. Zhu,[12,g] W. D. Zhu,[41] Y. C. Zhu,[72,58] Z. A. Zhu,[1,64] J. H. Zou,[1] and J. Zu[72,58]

(BESIII Collaboration)

[1]*Institute of High Energy Physics, Beijing 100049, People's Republic of China*
[2]*Beihang University, Beijing 100191, People's Republic of China*
[3]*Bochum Ruhr-University, D-44780 Bochum, Germany*
[4]*Budker Institute of Nuclear Physics SB RAS (BINP), Novosibirsk 630090, Russia*
[5]*Carnegie Mellon University, Pittsburgh, Pennsylvania 15213, USA*
[6]*Central China Normal University, Wuhan 430079, People's Republic of China*
[7]*Central South University, Changsha 410083, People's Republic of China*
[8]*China Center of Advanced Science and Technology, Beijing 100190, People's Republic of China*
[9]*China University of Geosciences, Wuhan 430074, People's Republic of China*
[10]*Chung-Ang University, Seoul 06974, Republic of Korea*
[11]*COMSATS University Islamabad, Lahore Campus, Defence Road, Off Raiwind Road, 54000 Lahore, Pakistan*
[12]*Fudan University, Shanghai 200433, People's Republic of China*
[13]*GSI Helmholtzcentre for Heavy Ion Research GmbH, D-64291 Darmstadt, Germany*
[14]*Guangxi Normal University, Guilin 541004, People's Republic of China*
[15]*Guangxi University, Nanning 530004, People's Republic of China*
[16]*Hangzhou Normal University, Hangzhou 310036, People's Republic of China*
[17]*Hebei University, Baoding 071002, People's Republic of China*
[18]*Helmholtz Institute Mainz, Staudinger Weg 18, D-55099 Mainz, Germany*
[19]*Henan Normal University, Xinxiang 453007, People's Republic of China*
[20]*Henan University, Kaifeng 475004, People's Republic of China*
[21]*Henan University of Science and Technology, Luoyang 471003, People's Republic of China*
[22]*Henan University of Technology, Zhengzhou 450001, People's Republic of China*
[23]*Huangshan College, Huangshan 245000, People's Republic of China*
[24]*Hunan Normal University, Changsha 410081, People's Republic of China*
[25]*Hunan University, Changsha 410082, People's Republic of China*
[26]*Indian Institute of Technology Madras, Chennai 600036, India*
[27]*Indiana University, Bloomington, Indiana 47405, USA*
[28a]*INFN Laboratori Nazionali di Frascati, I-00044 Frascati, Italy*
[28b]*INFN Sezione di Perugia, I-06100, Perugia, Italy*
[28c]*University of Perugia, I-06100, Perugia, Italy*
[29a]*INFN Sezione di Ferrara, I-44122 Ferrara, Italy*
[29b]*University of Ferrara, I-44122 Ferrara, Italy*
[30]*Inner Mongolia University, Hohhot 010021, People's Republic of China*
[31]*Institute of Modern Physics, Lanzhou 730000, People's Republic of China*
[32]*Institute of Physics and Technology, Peace Avenue 54B, Ulaanbaatar 13330, Mongolia*
[33]*Instituto de Alta Investigación, Universidad de Tarapacá, Casilla 7D, Arica 1000000, Chile*
[34]*Jilin University, Changchun 130012, People's Republic of China*
[35]*Johannes Gutenberg University of Mainz, Johann-Joachim-Becher-Weg 45, D-55099 Mainz, Germany*
[36]*Joint Institute for Nuclear Research, 141980 Dubna, Moscow region, Russia*
[37]*Justus-Liebig-Universitaet Giessen, II. Physikalisches Institut, Heinrich-Buff-Ring 16, D-35392 Giessen, Germany*
[38]*Lanzhou University, Lanzhou 730000, People's Republic of China*
[39]*Liaoning Normal University, Dalian 116029, People's Republic of China*
[40]*Liaoning University, Shenyang 110036, People's Republic of China*
[41]*Nanjing Normal University, Nanjing 210023, People's Republic of China*
[42]*Nanjing University, Nanjing 210093, People's Republic of China*
[43]*Nankai University, Tianjin 300071, People's Republic of China*
[44]*National Centre for Nuclear Research, Warsaw 02-093, Poland*
[45]*North China Electric Power University, Beijing 102206, People's Republic of China*
[46]*Peking University, Beijing 100871, People's Republic of China*
[47]*Qufu Normal University, Qufu 273165, People's Republic of China*
[48]*Renmin University of China, Beijing 100872, People's Republic of China*
[49]*Shandong Normal University, Jinan 250014, People's Republic of China*

[50]Shandong University, Jinan 250100, People's Republic of China
[51]Shanghai Jiao Tong University, Shanghai 200240, People's Republic of China
[52]Shanxi Normal University, Linfen 041004, People's Republic of China
[53]Shanxi University, Taiyuan 030006, People's Republic of China
[54]Sichuan University, Chengdu 610064, People's Republic of China
[55]Soochow University, Suzhou 215006, People's Republic of China
[56]South China Normal University, Guangzhou 510006, People's Republic of China
[57]Southeast University, Nanjing 211100, People's Republic of China
[58]State Key Laboratory of Particle Detection and Electronics, Beijing 100049, Hefei 230026, People's Republic of China
[59]Sun Yat-Sen University, Guangzhou 510275, People's Republic of China
[60]Suranaree University of Technology, University Avenue 111, Nakhon Ratchasima 30000, Thailand
[61]Tsinghua University, Beijing 100084, People's Republic of China
[62a]Turkish Accelerator Center Particle Factory Group, Istinye University, 34010 Istanbul, Turkey
[62b]Near East University, Nicosia, North Cyprus, 99138, Mersin 10, Turkey
[63]H H Wills Physics Laboratory, University of Bristol, Tyndall Avenue, Bristol BS8 1TL, United Kingdom
[64]University of Chinese Academy of Sciences, Beijing 100049, People's Republic of China
[65]University of Groningen, NL-9747 AA Groningen, The Netherlands
[66]University of Hawaii, Honolulu, Hawaii 96822, USA
[67]University of Jinan, Jinan 250022, People's Republic of China
[68]University of Manchester, Oxford Road, Manchester M13 9PL, United Kingdom
[69]University of Muenster, Wilhelm-Klemm-Strasse 9, 48149 Muenster, Germany
[70]University of Oxford, Keble Road, Oxford OX13RH, United Kingdom
[71]University of Science and Technology Liaoning, Anshan 114051, People's Republic of China
[72]University of Science and Technology of China, Hefei 230026, People's Republic of China
[73]University of South China, Hengyang 421001, People's Republic of China
[74]University of the Punjab, Lahore-54590, Pakistan
[75a]University of Turin, I-10125 Turin, Italy
[75b]University of Eastern Piedmont, I-15121 Alessandria, Italy
[75c]INFN, I-10125 Turin, Italy
[76]Uppsala University, Box 516, SE-75120 Uppsala, Sweden
[77]Wuhan University, Wuhan 430072, People's Republic of China
[78]Yantai University, Yantai 264005, People's Republic of China
[79]Yunnan University, Kunming 650500, People's Republic of China
[80]Zhejiang University, Hangzhou 310027, People's Republic of China
[81]Zhengzhou University, Zhengzhou 450001, People's Republic of China

[a]Deceased.
[b]Also at the Moscow Institute of Physics and Technology, Moscow 141700, Russia.
[c]Also at the Novosibirsk State University, Novosibirsk 630090, Russia.
[d]Also at the NRC "Kurchatov Institute," PNPI, 188300 Gatchina, Russia.
[e]Also at Goethe University Frankfurt, 60323 Frankfurt am Main, Germany.
[f]Also at Key Laboratory for Particle Physics, Astrophysics and Cosmology, Ministry of Education; Shanghai Key Laboratory for Particle Physics and Cosmology; Institute of Nuclear and Particle Physics, Shanghai 200240, People's Republic of China.
[g]Also at Key Laboratory of Nuclear Physics and Ion-Beam Application (MOE) and Institute of Modern Physics, Fudan University, Shanghai 200443, People's Republic of China.
[h]Also at State Key Laboratory of Nuclear Physics and Technology, Peking University, Beijing 100871, People's Republic of China.
[i]Also at School of Physics and Electronics, Hunan University, Changsha 410082, China.
[j]Also at Guangdong Provincial Key Laboratory of Nuclear Science, Institute of Quantum Matter, South China Normal University, Guangzhou 510006, China.
[k]Also at MOE Frontiers Science Center for Rare Isotopes, Lanzhou University, Lanzhou 730000, People's Republic of China.
[l]Also at Lanzhou Center for Theoretical Physics, Lanzhou University, Lanzhou 730000, People's Republic of China.
[m]Also at the Department of Mathematical Sciences, IBA, Karachi 75270, Pakistan.
[n]Also at Ecole Polytechnique Federale de Lausanne (EPFL), CH-1015 Lausanne, Switzerland.
[o]Also at Helmholtz Institute Mainz, Staudinger Weg 18, D-55099 Mainz, Germany.
[p]Also at School of Physics, Beihang University, Beijing 100191, China.